Dynamics of postnatal bone development and epiphyseal synostosis in the caprine autopod

Christopher J. Panebianco[1,2,3], Maha Essaidi[1,2,3], Elijah Barnes[1,2,4], Ashley Williams [1,2,4], Karin Vancíková[5,6], Margot C. Labberté[7], Pieter Brama[7], Niamh C. Nowlan[5,6,*], Joel D. Boerckel[1,2,3,*]

[1]Department of Orthopaedic Surgery, University of Pennsylvania, Philadelphia, PA, USA
[2]Center for Engineering Mechanobiology, University of Pennsylvania, Philadelphia, PA, USA
[3]Department of Bioengineering, University of Pennsylvania, Philadelphia, PA, USA
[4]School of Science, Technology, Engineering, and Mathematics, Alabama State University, Montgomery, AL, USA
[5]School of Mechanical and Materials Engineering, University College Dublin, Dublin, Ireland
[6]UCD Conway Institute, University College Dublin, Dublin, Ireland
[7]Translational Research Unit, School of Veterinary Medicine, University College Dublin, Dublin, Ireland

*Corresponding authors:

Niamh C. Nowlan
University College Dublin
UCD School of Mechanical and Materials Engineering
Belfied, Dublin 4, Ireland
+353 1 716 1735 (Phone)
niamh.nowlan@ucd.ie (Email)

Joel D. Boerckel
University of Pennsylvania
Department of Orthopaedic Research
Department of Bioengineering
376A Stemmler Hall
3450 Hamilton Walk
Philadelphia, PA 19104-6081
215-746-8168 (Phone)
boerckel@pennmedicine.upenn.edu (Email)

Abstract

Bones develop to structurally balance strength and mobility. Bone developmental dynamics are influenced by whether an animal is ambulatory at birth (*i.e.*, precocial). Precocial species, such as goats, develop advanced skeletal maturity in utero, making them useful models for studying the dynamics of bone formation under mechanical load. Here, we used microcomputed tomography and histology to characterize postnatal bone development in the autopod of the caprine lower forelimb. The caprine autopod features two toes, fused by metacarpal synostosis (*i.e.*, bone fusion) prior to birth. Our analysis focused on the phalanges 1 (P1) and metacarpals of the goat autopod from birth through adulthood (3.5 years). P1 cortical bone densified rapidly after birth (half-life using one-phase exponential decay model ($\tau_{1/2}$ = 1.6 ± 0.4 months), but the P1 cortical thickness increased continually through adulthood ($\tau_{1/2}$ = 7.2 ± 2.7 mo). Upon normalization by body mass, the normalized polar moment of inertia of P1 cortical bone was constant over time, suggestive of structural load adaptation. P1 trabecular bone increased in trabecular number ($\tau_{1/2}$ = 6.7 ± 2.8 mo) and thickness ($\tau_{1/2}$ = 6.6 ± 2.0 mo) until skeletal maturity, while metacarpal trabeculae grew primarily through trabecular thickening ($\tau_{1/2}$ = 7.9 ± 2.2 mo). Unlike prenatal fusion of the metacarpal diaphysis, synostosis of the epiphyses occurred postnatally, prior to growth plate closure, through a unique fibrocartilaginous endochondral ossification. These findings implicate ambulatory loading in postnatal bone development of precocial goats and identify a novel postnatal synostosis event in the caprine metacarpal epiphysis.

Keywords: Caprine, Bone Development, Bone Morphometry, Microcomputed Tomography, Bone Fusion

1.0 Introduction

The skeleton continuously remodels throughout mammalian growth and development, creating a structure optimized for high strength and low weight. While we have long known that mature bone adapts and remodels based on loading (Wolff 1893; Frost 1994), it has been difficult to decouple early bone development programs from adaptation to ambulatory loading. As precocial species, goats are ambulatory at birth, providing continuous loading during skeletal growth. Here, we mapped the developmental dynamics of the autopod of the caprine lower forelimb from birth through adulthood, focusing on the phalanges 1 (P1) and metacarpal bones in the autopod.

An animal's ability to ambulate at birth influences the dynamics of postnatal skeletal development. Humans, mice, and rats are examples of altricial species, meaning they are non-ambulatory at birth. Altricial species initiate primary ossification in utero, under conditions of dynamic fetal movement (Nowlan 2015; Beall et al. 2007; Kozhemyakina et al. 2015; Collins et al. 2024), then the majority of secondary ossification centers initiate after birth (Kozhemyakina et al. 2015; Breeland et al. 2024; Gardner and Gray 1970). Unlike altricial species, precocial species such as goats, horses, and sheep, ambulate from birth through adulthood (**Fig. 1**) and undergo primary and secondary ossification in utero as an anticipatory mechanism to prepare for future loading (Gorissen et al. 2016; Skedros et al. 2004; Skedros et al. 2007). It has been hypothesized that this early secondary ossification evolved to support the physis to withstand high mechanical loading shortly after birth (Xie et al. 2020). Though previous research has described gestational bone development of precocial species, few studies have investigated their postnatal development. Understanding postnatal developmental dynamics in precocial species may inform how mechanical cues influence skeletal morphogenesis.
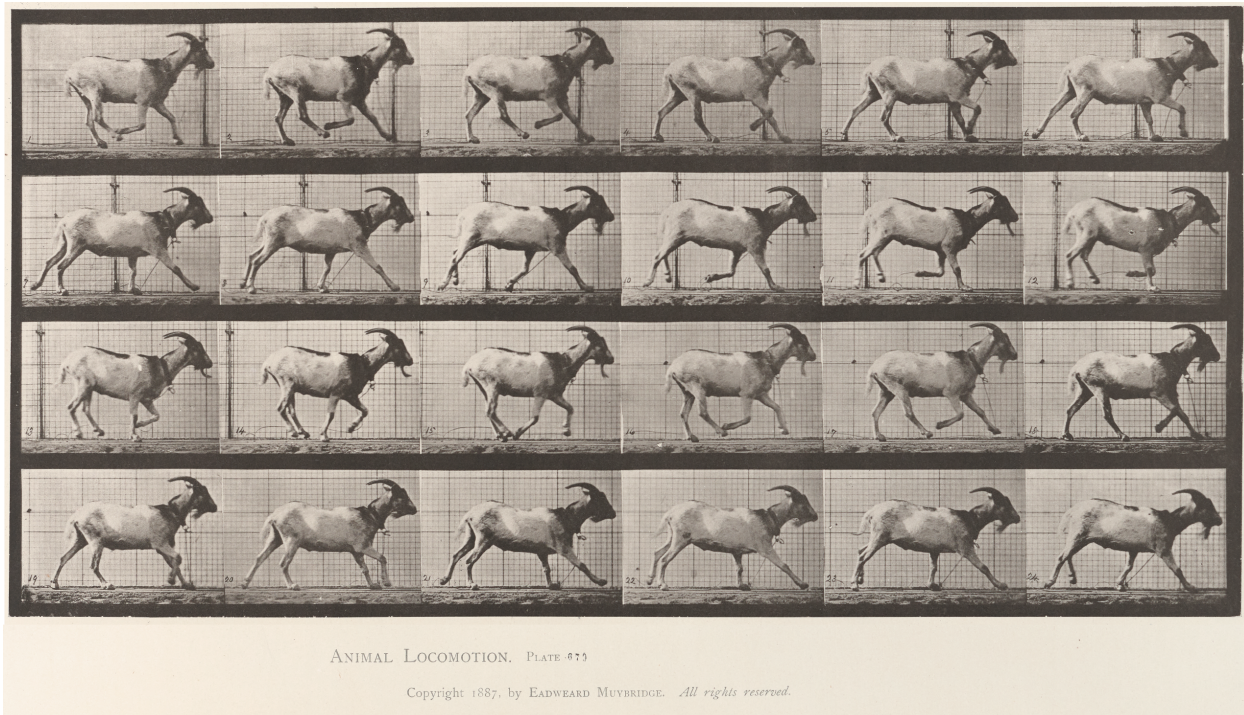
ANIMAL LOCOMOTION. PLATE 676

Copyright 1887, by EADWEARD MUYBRIDGE. *All rights reserved.*

Figure 1. Goats are precocial animals that ambulate from birth through adulthood. Reproduction of 1887 Animal Locomotion Plate 676, captured by Eadweard Muybridge at the University of Pennsylvania. Plates provided by the University of Pennsylvania University Archives and Records Center.

Diaphyseal synostosis has evolved in a variety of species, likely to provide structural resistance to high bending forces. For example, the jerboa, a bipedal rodent, evolved fused metatarsal bones that reduce peak bone stresses and provide a factor-of-safety to the hindlimb during bipedal ambulation (Villacís Núñez et al. 2022). This evolutionary advantage contributes to the jerboa's ability to jump ten-times its hip-height and withstand peak ground-reaction forces that are five-times its body weight (Moore et al. 2017; Biewener 1989). As altricial species with limited hindlimb loading immediately after birth, jerboa metatarsal synostosis occurs postnatally (Gutierrez et al. 2019; Cooper et al. 2014). Diaphyseal synostosis is also observed in some precocial species. For example, each goat forelimb has two independent metacarpal rudiments embryonically, but these rudiments undergo diaphyseal synostosis in utero to form one metacarpal bone at birth. As distal elements (*e.g.,* autopod) mature later in development than the more proximal zeugopod and stylopod, evolutionary reasoning suggests that the ungulate diaphyseal synostosis initiates in utero to provide increased strength and enable locomotion at birth (Leinders and Sondaar 1973). It remains unknown whether these fusion events continue through postnatal development. These findings may be useful for understanding how biomechanical pressures guide adaptation in precocial species.

4

Here, we characterize the dynamics of postnatal bone development and epiphyseal synostosis in the caprine autopod from birth through adulthood. P1 cortical bone rapidly densified, then became continually thicker until skeletal maturity, with structural distribution determined by ambulatory loading. Simultaneously, P1 trabecular bone increased in trabecular number and thickness until skeletal maturity, while metacarpal trabecular number was constant and the network grew through trabecular thickening. Metacarpal synostosis began *in utero*; however, the epiphyses did not begin to fuse until after 1.5 months postnatally. Histological analyses indicated that this epiphyseal synostosis occurred through fibrocartilaginous endochondral ossification, prior to growth plate closure. Together, these data provide new insights into precocial bone development under ambulatory loading.

2.0 Materials and methods

2.1 Study design

We performed bone morphometry on the autopods of the lower forelimbs of 44 goats at the following ages: 3 days (3D, N=6 male, N=3 female), 1.5 months (1.5M, N=3 male, N=3 female), 3M (N=1 male, N=4 female), 6M (N=6 female), 9M (N=3 male, N=3 female), 12M (N=3 male, N=3 female), and 3.5 years (3.5Y, N=6 female). Each animal was considered an experimental unit and goats were assigned to groups in cohorts. Goats were continually assessed by a veterinarian, and only animals in good physical health were included in the study. At the specified timepoints, animals were euthanized and the phalanges 1 (P1) and metacarpal bones were harvested from autopods of the lower forelimbs for microcomputed tomography (µCT) and histological analyses.

2.2 Animal husbandry and care

This animal experiment complied with the ARRIVE guidelines. Ethical evaluation and approval were provided by the Animal Research Ethics Committee (AREC-21-22) of University College Dublin (UCD) and the Lyons UCD Research Farm Animal Welfare Board (Health, Husbandry and Monitoring plans: 201,907). Animals were selected at predetermined age points from the Translational Research Unit (TRU) goat herd at University College Dublin Lyons Research Farm (Breeding license AREC-22-408929). In principle all animals genetically originated from the same high health closed goat herd of our sole supplier.

The TRU goat herds were kept under normal goat husbandry conditions. Herds had loose housing and pasture access when weather conditions were appropriate. Daily health checks of the herd were performed by appropriately trained husbandry staff, with weather conditions and barn climate parameters documented on the daily health check sheets. Animals were reared with their respective mothers when available or at a lambing bar with milk replacer to suckle milk until weaning at approximately 60-90 days (depending on body condition score and weight). Ad libitum concentrates and hay/silage were provided from approximately 14 days of age. After goats were 3 months, hay/silage remained ad libitum, but concentrates were provided based on their daily requirements and weight gain to prevent overfeeding. Veterinary staff of the TRU performed weekly monitoring health checks on the goat herds and were available 24/7 in case a veterinary consultation is required.

When animals reached their predetermined age endpoint, a normal general health check and orthopaedic assessment was conducted. Only animals that met these requirements were included in the study. Included animals underwent humane euthanasia under sedation with a barbiturate overdose. Following euthanasia, the P1 and metacarpal bones were harvested for microcomputed tomography (µCT) and histological analyses. Samples were fixed using 10% neutral buffered formalin (NBF) for 3 days, then 5% NBF for 3 weeks. Fixed samples were washed with 1X phosphate buffered saline (PBS), then frozen at -20°C in a solution of 30% sucrose (w/v) in 1X PBS prior to analyses.

2.3 Microcomputed tomography (µCT)

The night before scanning, frozen samples were thawed overnight at 4°C. Thawed samples were wrapped in PBS-soaked gauze and scanned using a SCANCO µCT 45 desktop microCT scanner (SCANCO Medical, Wangen-Brüttisellen, Switzerland). X-ray images were acquired using x-ray intensity of 145 µA, energy of 55 kVp, integration time of 400 ms, and resolution of 10.4 µm. Reconstructed scans were semi-automatically contoured and analyzed using the SCANCO microCT image analysis interface (SCANCO Medical) according to morphometric standards (Bouxsein et al. 2010).

For P1 bones, approximately 200 slices of the midshaft cortical region were contoured to measure cortical tissue cross-sectional area (Tt.Ar), cortical bone area (Ct.Ar), cortical area fraction (Ct.Ar/Tt.Ar), cortical thickeness (Ct.Th), tissue mineral density (TMD), and polar moment of inertia (J). Additionally, the entire P1 distal trabecular

region was contoured to measure trabecular bone volume (BV/TV), trabecular number (Tb.N), trabecular thickness (Tb.Th), and trabecular separation (Tb.Sp). For each goat, the cortical and trabecular outcome measurements were averaged for the medial and lateral P1 bones, so each goat was an experimental unit.

For metacarpal bones, BV/TV, Tb.N, Tb.Th, and Tb.Sp were calculated for the combined distal trabecular network in both epiphyses. Additionally, the maximum epiphyseal fusion length was calculated for each metacarpal bones using the mid-sagittal virtual slice numbers for the initiation of epiphyseal synostosis and the physis.

2.4 Histology

Representative P1 and metacarpal samples (N=3 per timepoint) were used for paraffin histology. P1 samples were decalcified for 3.5 weeks using Formical-4 Decalcifier (StatLab Medical Products, McKinney, Texas, USA), with weekly reagent changes. Metacarpal samples were decalcified for 4 weeks using Formical-4, then an additional 2 weeks using Formical-2000 (StatLab Medical Products), with weekly reagent changes. Decalcified samples were trimmed using a Tissue-Tek® Accu-Edge® Trimming Knife (Electron Microscope Sciences, Hatfield, PA, USA) and processed for paraffin histology using a Thermo Scientific Excelsior AS Tissue Processor (Thermo Fisher Scientific, Waltham, MA). Processed samples were paraffin-embedded and sectioned to 10 µm using a Leica RM 2030 Microtome (Leica, Bala Cynwyd, PA, USA). Sections were stained for safranin-O/fast green using standard protocols. Stained sections were imaged using a ZEISS Axio Scan.Z1 Slide Scanner (ZEISS, Oberkochen, Germany).

2.5 Statistical analysis

The "pwr2" package in R (Indianapolis, IN, USA) was used to conduct a power analysis for large effect sizes (α=0.05, β=0.20, f = 0.4-0.6). GraphPad Prism software Version 10.3.1 (GraphPad Software, San Diego, CA, USA) was used to conduct all statistical analyses. A one-way analysis of variance (ANOVA) with Tukey's multiple comparison test was used to determine significant differences in all outcome measurements over developmental time. Prism was also used to fit all outcome measurements with a one-phase exponential decay model ($y = span * e^{-k/t} + plateau$). Graphical results are reported as a one-phase decay model with the goodness of fit (R^2) and half-life ($\tau_{1/2}$). $\tau_{1/2}$ is the amount of developmental time, in months, for each outcome to achieve 50% of its maximum value.

3.0 Results

3.1 Phalanges 1 (P1) postnatal development dynamics

Phalanges 1 (P1) bones showed significant increases in all outcomes for cortical bone morphometry over postnatal development (**Fig. 2**). To better understand the dynamics of caprine P1 development over time, each outcome measurement was fit with a one-phase exponential decay model. Curves fit well for all outcomes with coefficients of determination (R^2) values between 0.62 - 0.91 (**Fig. 2B-G**). By extracting the half-life values ($\tau_{1/2}$) from these curves, we could determine the characteristic time scale for each outcome. Outcomes with lower $\tau_{1/2}$ values achieved 50% of their maximum value earlier in developmental time than outcomes with higher $\tau_{1/2}$ values. Thus, outcomes with lower $\tau_{1/2}$ values achieved their maximum value faster and the outcome plateaued earlier in developmental time than outcomes with higher $\tau_{1/2}$ values. Cortical area fraction (Ct.Ar/Tt.Ar, $\tau_{1/2}$ = 1.0 ± 0.3 mo, **Fig. 2D**), a measure of cortical porosity, and tissue mineral density (TMD, $\tau_{1/2}$ = 1.6 ± 0.4 mo, **Fig. 2E**) plateaued most rapidly. Total cross-sectional area (Tt.Ar, $\tau_{1/2}$ = 4.8 ± 1.7 mo, **Fig. 2B**), cortical bone area (Ct.Ar, $\tau_{1/2}$ = 6.0 ± 2.6 mo, **Fig. 2C**), cortical thickness (Ct.Th, $\tau_{1/2}$ = 7.2 ± 2.7 mo, **Fig. 2F**), and polar moment of inertia (*J*, $\tau_{1/2}$ = 4.3 ± 1.9 mo, **Fig. 2G**) plateaued less rapidly and continued to increase through 12 months. These results indicate that P1 bones undergo early cortical condensation followed by progressive cortical thickening into adulthood.
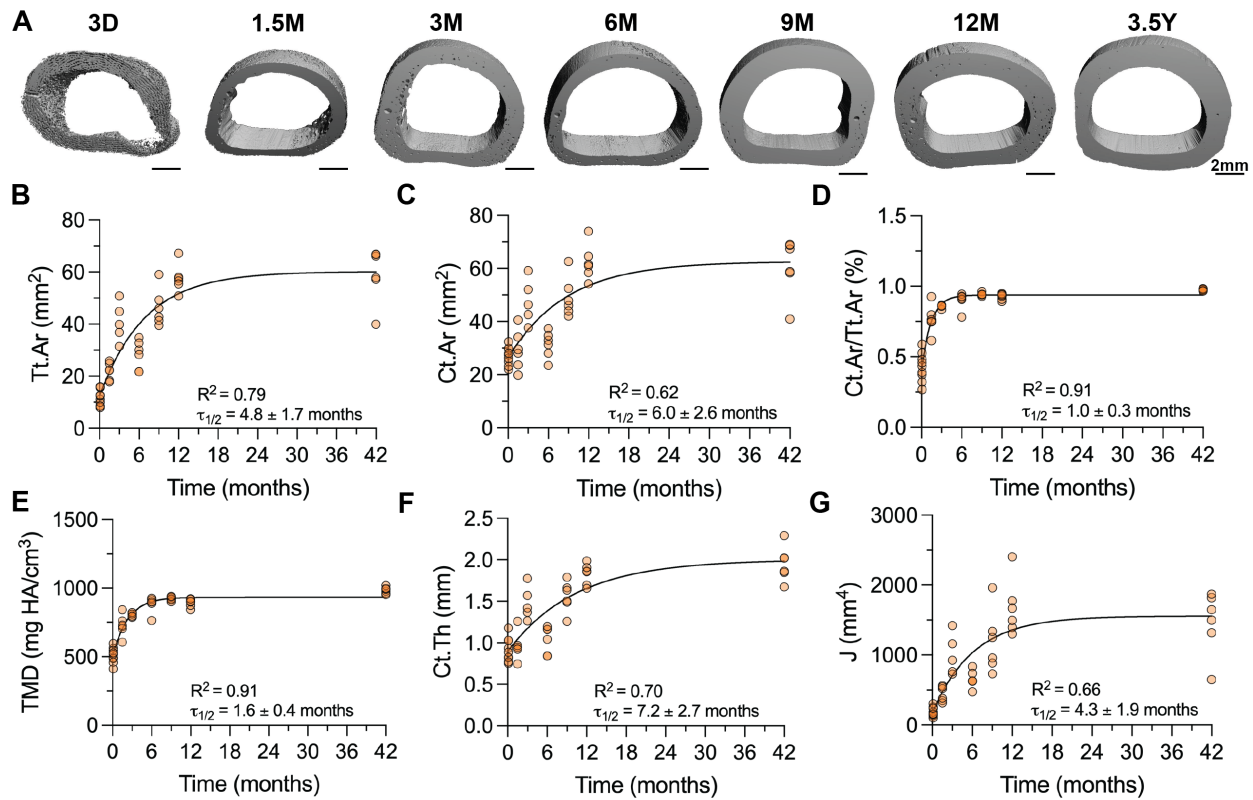
8

Figure 2. Phalanges 1 (P1) cortices exhibit rapid condensation and continuous expansion until adulthood. (A) Transverse views of 3D microcomputed tomography (microCT) reconstructions of P1 cortical mid-shaft. Scale bars = 2 mm. (B) Cortical tissue cross-sectional area (Tt.Ar), (C) Cortical bone area (Ct.Ar), (D) Cortical area fraction (Ct.Ar/Tt.Ar), (E) Tissue mineral density (TMD), (F) Cortical thickness (Ct.Th), and (G) Polar moment of inertia (J) throughout developmental time, fit with a one-phase decay model. Goodness of fit (R^2) and half-life ($\tau_{1/2}$) are reported for each graph. D = days of age, M = months of age, Y = years of age.

P1 distal trabecular microarchitecture also showed significant changes in all outcomes over postnatal development (**Fig. 3**). Trabecular number (Tb.N, $\tau_{1/2}$ = 6.7 ± 2.8 mo, **Fig. 3B**) and trabecular thickness (Tb.Th, $\tau_{1/2}$ = 6.6 ± 2.0 mo, **Fig. 3C**) increased continuously through 12 months. As a result of this increased formation of new trabecular networks and growth of existing trabecular networks, the bone volume fraction (BV/TV, $\tau_{1/2}$ = 3.3 ± 1.0 mo, **Fig. 3D**) increased and the trabecular separation (Tb.Sp, $\tau_{1/2}$ = 7.9 ± 3.2 mo, **Fig. 3E**) decreased continuously through 12 months. Simultaneously, the existing trabeculae were increasing in mineralization, as shown by the continuous changes in TMD ($\tau_{1/2}$ = 4.2 ± 1.7 mo, **Fig. 3F**). Curves fit well for all outcomes with R^2 values between 0.63 - 0.85 (Fig. 3B-F). These data suggest that P1 postnatal cancellous bone formation is characterized by both the formation of new trabecular networks and the growth of existing trabecular networks.
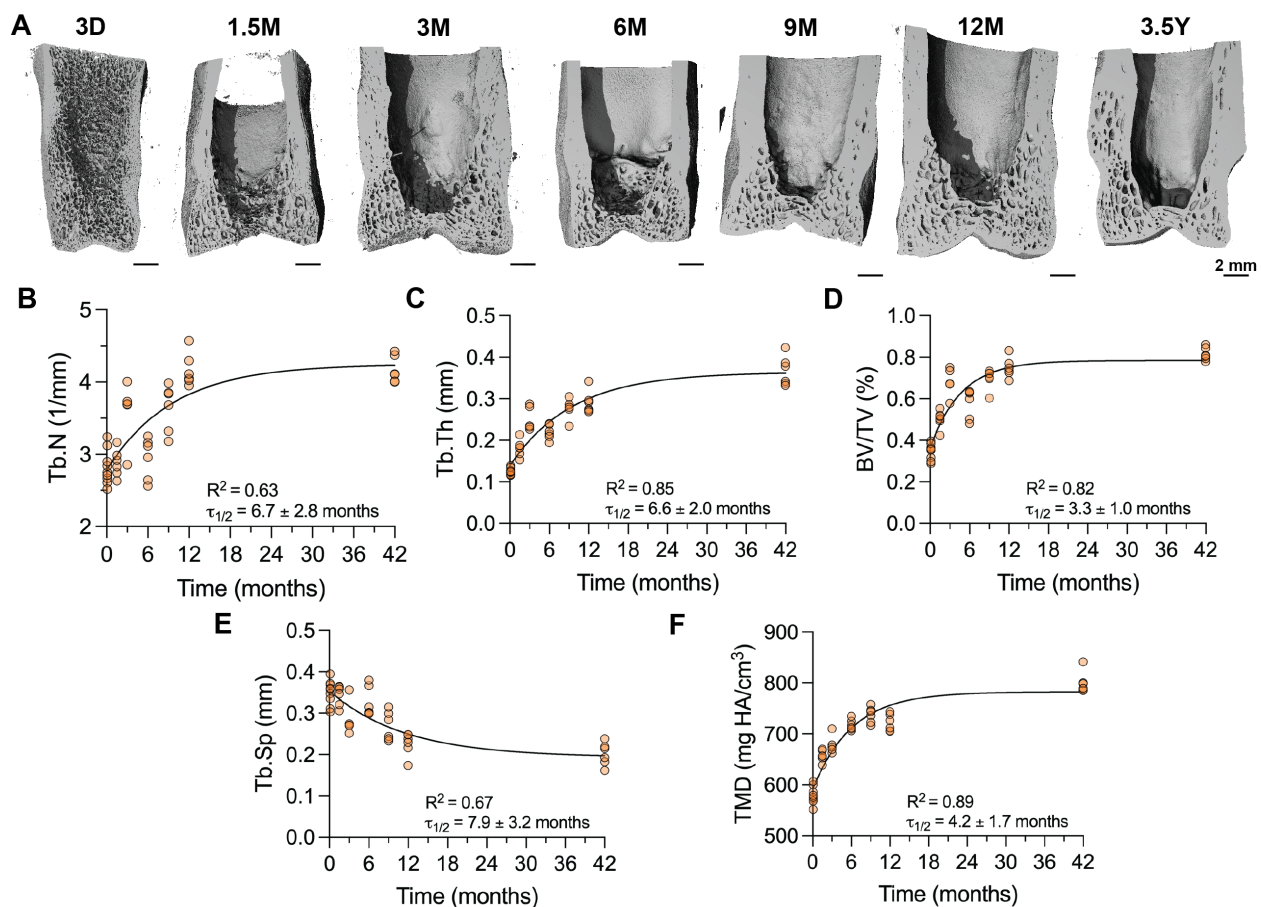
Figure 3. Distal P1 bones grow by formation of new trabeculae and expansion of existing trabeculae. (A) Transverse views of 3D microCT reconstructions of P1 bones with a virtual slice through the mid-coronal plane using microCT. Scale bars = 2 mm. (B) Trabecular number (Tb.N), (C) Trabecular thickness (Tb.Th), (D) Bone volume fraction (BV/TV), (E) Trabecular spacing (Tb.Sp), and (F) Tissue mineral density (TMD) throughout developmental time, fit with a one-phase decay model. Goodness of fit (R^2) and half-life ($\tau_{1/2}$) are reported for each graph. D = days of age, M = months of age, Y = years of age.

P1 bone structure formed concurrently with precocial ambulatory weight-bearing. Animals increased continuously in mass from birth through adulthood ($\tau_{1/2}$ = 5.1 ± 1.2 mo, **Fig. 4A**). To determine how bone morphometry adapted with loading, we normalized cortical and trabecular outcomes by animal body mass. Body mass-normalized Ct.Ar ($\tau_{1/2}$ = 0.9 ± 0.4 mo, **Fig. 4B**), cortical TMD ($\tau_{1/2}$ = 1.4 ± 0.5 mo, **Fig. 4C**), BV/TV ($\tau_{1/2}$ = 1.5 ± 0.5 mo, **Fig. 4E**), and Tb.Th ($\tau_{1/2}$ = 1.3 ± 0.5 mo, **Fig. 4F**) all plateaued rapidly. In contrast, the body mass-normalized polar moment of inertia (*J/mass*) was constant over time (**Fig. 4D**). These data suggest that while bone accrual was dominated by animal growth rather than load-adaptation, the morphodynamics of cross-sectional distribution, indicative of structure resistance to bending and torsional loading, were adaptive to ambulatory loads.
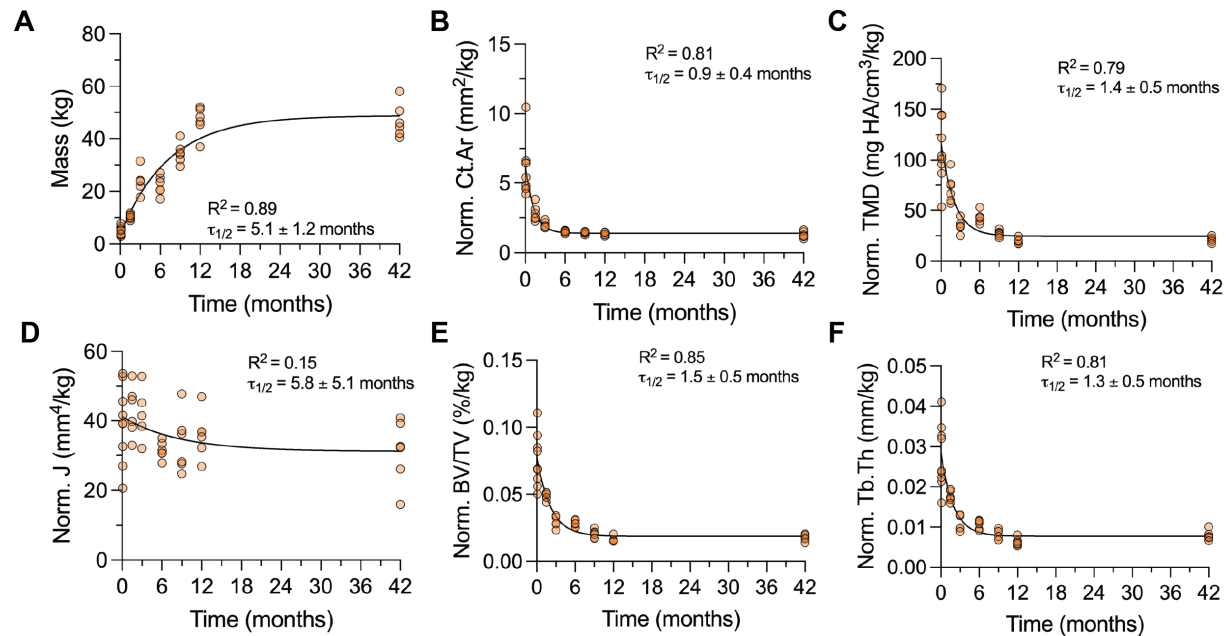
10

Figure 4. Morphodynamics of P1 cross-sectional distribution are adaptive to ambulatory loads. (A) *Animal mass throughout developmental time. Body mass normalized (B) Cortical bone area (Ct.Ar), (C) Cortical tissue mineral density (TMD), (D) Polar moment of inertia (J), (E) Trabecular bone volume fraction (BV/TV), and (F) Trabecular thickness (Tb.Th). Prefix "Norm" indicates outcome is normalized to animal mass. Data graphed as individual data points vs. time fit with a one-phase decay model. Goodness of fit (R^2) and half-life ($\tau_{1/2}$) are reported for each graph.*

3.2 Metacarpal postnatal development dynamics

Synostosis of the metaphyseal diaphyses was uniformly present in neonates, indicating fusion during fetal development (**Fig. 5A**). Cortical fusion was only observed in the diaphyseal region of the metacarpals and preserved the structure of two distinct distal physes. Additionally, metacarpal bones maintained distinct lateral and medial trabecular networks in the diaphysis and metaphysis.

Bone formation in the epiphyseal metacarpal trabecular bone occurred by increasing trabecular thickness, rather than increasing trabecular number (**Fig. 5B-G**). Tb.N changed minimally during postnatal metacarpal development (**Fig. 5C**), while Tb.Th ($\tau_{1/2} = 7.9 \pm 2.2$ mo, **Fig. 5D**) increased continuously over 3.5 years, suggesting bone accrual on existing trabecular networks over time. Simultaneously, the trabecular bone matrix increased in mineral density, TMD ($\tau_{1/2} = 5.7 \pm 1.7$ mo, **Fig. 5F**). Despite limited changes in Tb.N, the continuously increasing Tb.Th was sufficient to increase trabecular BV/TV, but not Tb.Sp, over postnatal development ($\tau_{1/2} = 6.9 \pm 3.1$ mo, **Fig. 5E-F**). These findings suggest that the development of the epiphyseal

11

metacarpal trabecular microarchitecture may feature mineral apposition on trabecular networks present at birth, rather than de novo trabecular formation.
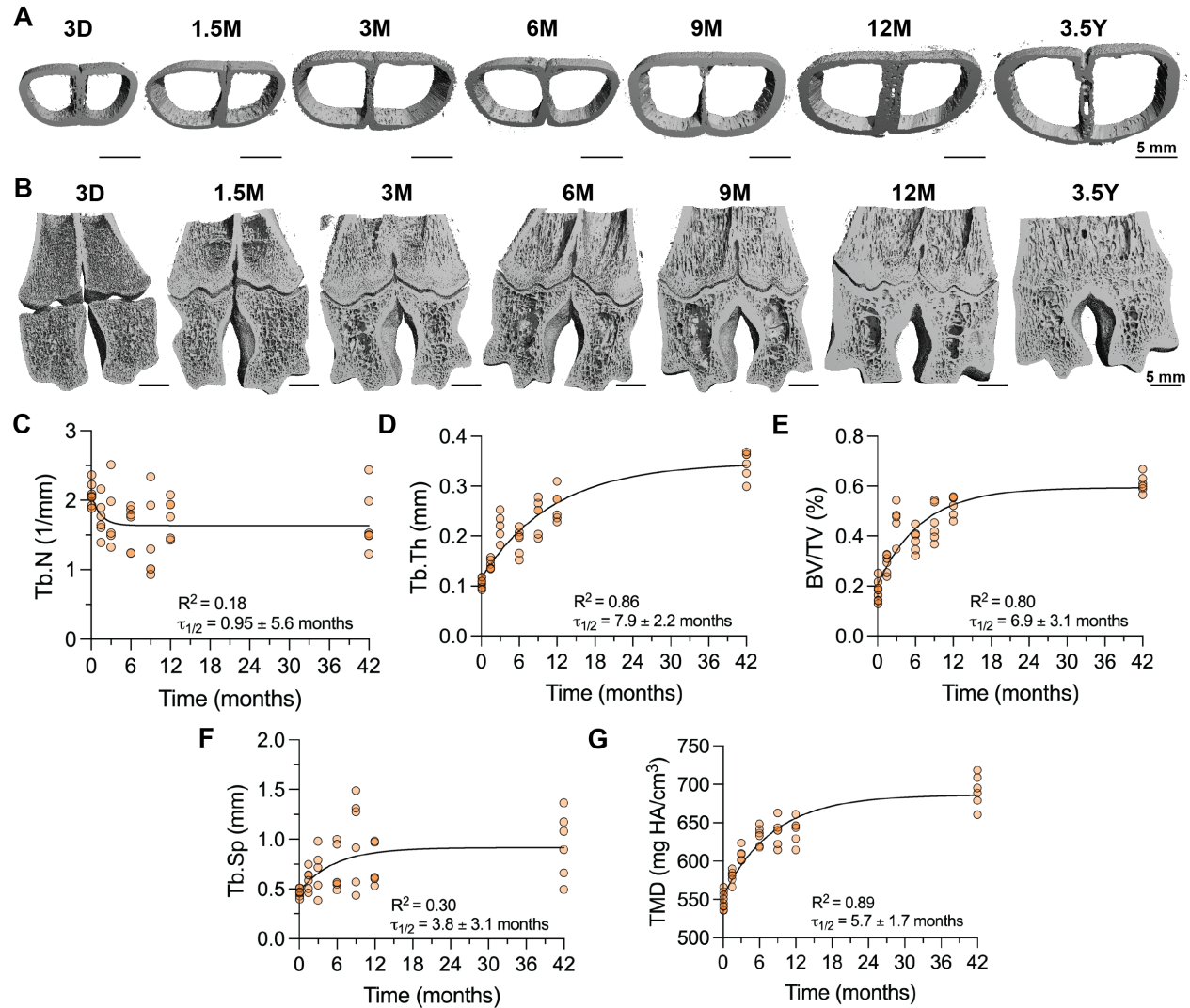

Figure 5. Metacarpal cortices fuse prior to birth and distal metacarpal trabecular bone grows through trabecular thickness expansion. (A) 3D microCT reconstructions of cortices with a virtual slice through the transverse plane, showing cortical fusion prior to birth. Scale bars = 5 mm. (B) 3D microCT reconstructions of metacarpal bones with a virtual slice through the mid-coronal plane. Scale bars = 5 mm. (C) Trabecular number (Tb.N), (D) Trabecular thickness (Tb.Th), (E) Bone volume fraction (BV/TV), (F) Trabecular spacing (Tb.Sp), and (G) Tissue mineral density (TMD) throughout developmental time, fit with a one-phase decay model. Goodness of fit (R^2) and half-life ($\tau_{1/2}$) are reported for each graph. D = days of age, M = months of age, Y = years of age.

3.3 Epiphyseal bone fusion dynamics in the metacarpal bones

Diaphyseal synostosis of the metacarpal bones occurred prenatally, but epiphyseal synostosis occurred postnatally. Diaphyseal synostosis could be observed as early as 3D (**Fig. 5A & 6A**), suggesting this fusion event

occurred prior to birth. In contrast, synostosis of the epiphyses distal to the growth plate did not initiate until after 3 months (**Fig. 6A & B**). We quantified the extent of epiphyseal synostosis as the fusion length, which increased continuously between 3 months and 12 months. The distal metacarpal physis closed between 12 months and 3.5 years; thus, it was not possible to measure fusion length past 12 months. At 3.5 years, the metacarpal bone remodeled the growth plate into a mature network of cancellous bone.
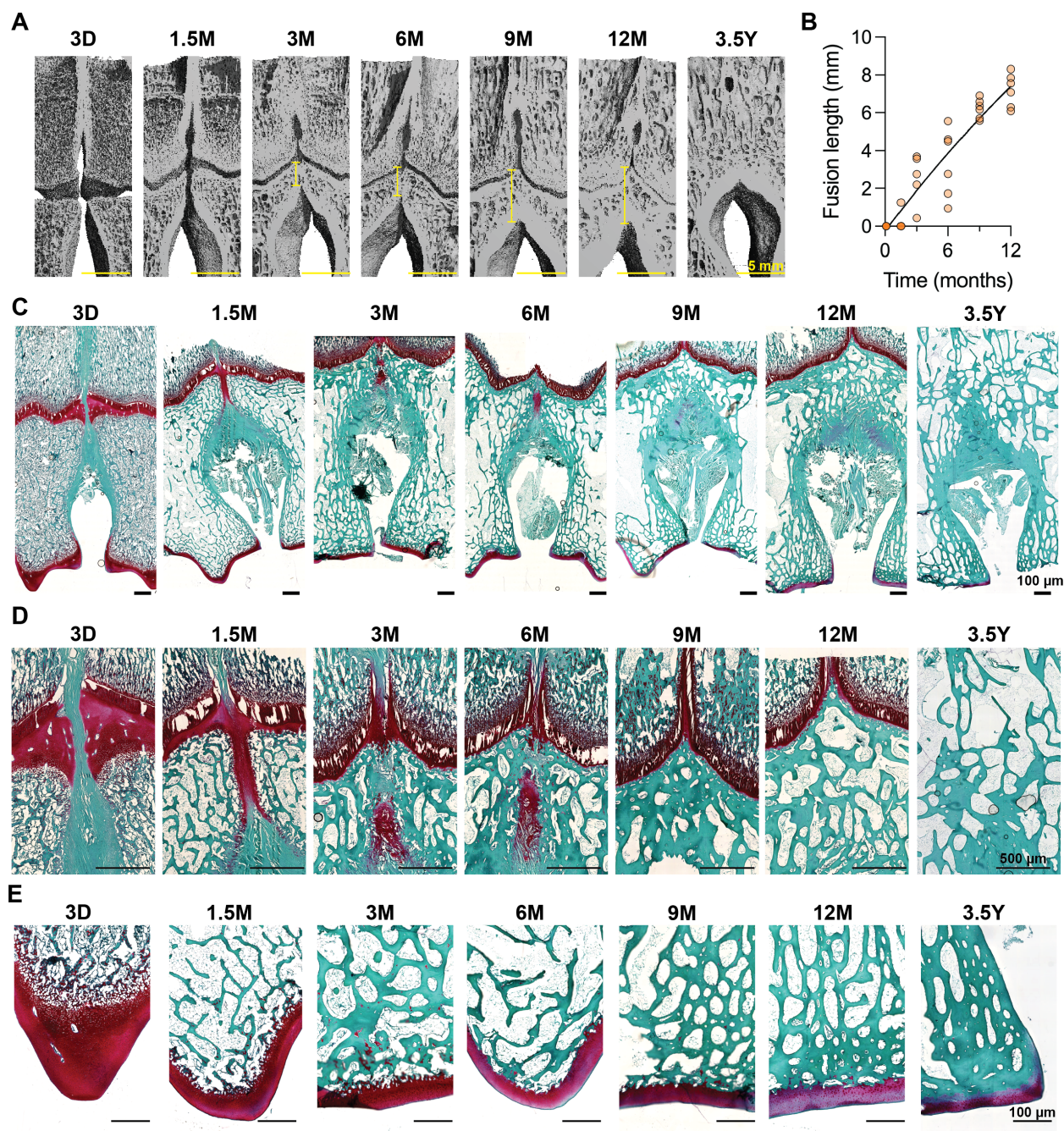

Figure 6. Metacarpal epiphyses are separated by a non-cartilaginous fibrous template at birth, but fuse by fibrocartilaginous endochondral ossification. (A) 3D microCT reconstructions of metacarpal bones with a virtual slice through the mid-coronal plane. Yellow line indicates extent of epiphyseal fusion (i.e., "fusion length"). Scale. bars = 5 mm.

(B) Quantification of the epiphyseal fusion length throughout developmental time. (C) Safranin o/fast green histological micrographs of metacarpal bones cut through the mid-coronal plane. Scale bars = 100 µm. (D) High-magnification micrographs of the distal metacarpus. Scale bars = 500 µm. (E) High-magnification micrographs of articular cartilage region of the metacarpus. Scale bars = 100 µm. D = days of age, M = months of age, Y = years of age.

Histological analyses showed how the distinct metacarpal epiphyses underwent synostosis. At 3 days, the metacarpus had two distinct growth plates (*i.e.,* physes) connected by a non-ossified, non-cartilaginous, periosteum-like fibrous tissue (**Fig. 6C & D**). Between 3 days and 1.5 months of age, the two physes joined and the previous fibrous tissue exhibited robust glycosaminoglycan (GAG) deposition, which continued through the epiphyseal region. Between 1.5 and 3 months, endochondral ossification initiated in the interstitial fibrocartilaginous matrix, starting at the border with the conjoined physes. This process led to epiphyseal synostosis by 9 months of age. From 9 to 12 months old, the metacarpals continued longitudinal growth. Throughout this epiphyseal synostosis, the physes maintained a fibrocartilaginous bridge, devoid of chondrocyte columns between physes. Between 12 months and 3.5 years, the physis closed and the distal metacarpal bone remodeled to form a singular continuous network of cancellous bone.

The articular cartilage also matured over postnatal development. At 3 days, the distal portion of the metacarpal bone exhibited a coherent articular cartilage surface with robust GAG content (**Fig. 6E**). The articular cartilage matured and condensed throughout postnatal development, forming superficial, transitional, and deep zones by 3 months of age and reduced GAG content by 12 months of age.

4.0 Discussion

Here, we characterized the dynamics of postnatal bone development and epiphyseal synostosis in the caprine autopod from birth through adulthood. P1 bone accrual was driven by growth patterning, while cross-sectional structural morphodynamics were maintained as ambulatory loading increased. While P1 distal trabeculae increased in thickness and number, metacarpal epiphyseal trabecular bone increased primarily by thickening of pre-existing trabeculae. The two bones that fuse to form the caprine metacarpus underwent diaphyseal synostosis, prenatally, but epiphyseal synostosis postnatally, prior to growth plate closure, through fibrocartilaginous endochondral ossification. Together, these data provide new insights into precocial bone development under ambulatory loading. Our findings may guide future caprine mechanobiology studies to mechanistically understand bone development and adaptation to ambulatory loading.

P1 cortical bone development was driven by both patterned growth and ambulatory loading. Cortical bone rapidly condensed within months, followed by continuous cortical bone accrual through adulthood. Notably, the body mass-normalized polar moment of inertia (*J*/mass) was maintained over developmental time, suggesting morphodynamic adaptation of structural distribution to resist bending deformation by ambulatory loading. These findings demonstrate the early functional capacity of the precocial skeleton, which persists into adulthood. The precocial skeleton develops so robustly that it can even develop normally after preterm birth and reduced birthweight (Magrini et al. 2023). In humans, which are altricial, peripubertal physical activity increases bone formation and establishes bone structural properties that maintain bone mass and strength (Palaiothodorou and Vagenas 2024; Weatherholt and Warden 2018), which persists into adulthood (Ducher et al. 2006; Warden et al. 2014). These findings support the notion that early and peripubertal impact loading can preserve adult bone strength and reduce fracture risk (Cooper et al. 2006; Ireland et al. 2014). Future studies can use the caprine model system to determine how altered perinatal mechanical loading impacts long-term skeletal health.

Trabecular architecture matured in P1 and metacarpal bones at different rates, but both were significantly different than altricial developmental dynamics. Trabecular bone only makes up 20% of total bone mass (Ott 2018), but the trabecular microarchitecture is crucial for determining bone mechanical properties (Liu et al. 2006; Ulrich et al. 1999). The developing caprine autopod of the lower forelimb is useful for studying adaptive trabecular bone growth because precocial species experience progressive biomechanical loading from gestation, through ambulation at birth, and into adulthood. Metacarpal distal epiphyseal BV/TV increased at a slower rate than P1 distal BV/TV, likely because metacarpal trabecular bone formed by trabecular bone apposition, rather than de novo trabecula formation. Since the metacarpal bone is more proximal than the P1 bone, it develops earlier in utero (Saunders 1948; Summerbell et al. 1973); thus, the metacarpal trabecular network may have formed in utero and only developed by bone accrual postnatally. Despite different mechanisms of development, trabecular BV/TV increased continuously after birth in the P1 and metacarpal bones, which is distinct from altricial trabecular bone dynamics. Altricial species experience a reduced loading state from birth until the onset of ambulation, which may explain the loss in trabecular bone volume fraction during early postnatal development (Acquaah et al. 2015). Once humans begin walking, trabecular BV/TV continuously increases coincidently with progressive loading (Ryan and Krovitz 2006; Gosman and Ketcham

2009). These post-ambulatory BV/TV increases mirror the progressive increases in trabecular bone observed in our study. Our findings contribute to the growing body of literature describing how precocial animals adapt to the biomechanical loading of ambulation (Gorissen et al. 2016; Skedros et al. 2004; Skedros et al. 2007).

The epiphyseal synostosis of the caprine metacarpal bones is distinct from other known mechanisms of endochondral bone formation or bone fusion. Here we show that the metacarpal physes and epiphyses are initially separated by a non-cartilaginous fibrous template, which becomes chondrogenic and subsequently undergoes fibrocartilaginous endochondral ossification. This rudimentary fibrous tissue is distinct from the cartilaginous rudiments that give rise to endochondral primary bone development (Berendsen and Olsen 2015), or the cartilage template that initiates the fibrocartilaginous enthesis (Killian 2022; Blitz et al. 2013; Sugimoto et al. 2013). The epiphyseal synostosis is also distinct from the fusion of flat bones of the skull. Like the metacarpal epiphyses, the sutures of the skull feature a flexible fibrous tissue, which allows for brain growth and development. However, suture fuse by intramembranous ossification, without a cartilaginous intermediate (Opperman 2000). Synostosis of metacarpal epiphyseal bone is perhaps most analogous to endochondral bone fracture healing (Bahney et al. 2019; Einhorn and Gerstenfeld 2015). The progression of fibrous to cartilaginous to bone tissue is like fracture healing, though fracture features an acute inflammatory phase and less robust fibrous tissue formation. Biomechanical stimuli are key regulators of endochondral ossification (Kozhemyakina et al. 2015; Collins et al. 2024), suture fusion (Khonsari et al. 2013; Sanchez-Lara et al. 2010), enthesis development (Killian 2022), and fracture healing (Goodship and Kenwright 1985; Matziolis et al. 2006; Herberg et al. 2019; McDermott et al. 2019; Kegelman et al. 2021) and may play a role in metacarpal epiphyseal synostosis. Interrogating the mechanical basis of metacarpal epiphyseal synostosis could lead to novel insights into the underlying mechanisms.

Together with a growing body of literature on precocial bone formation, these development dynamics data may form a foundation on which to uncover how mechanical forces regulate skeletal development, disease, and regeneration. One limitation of this study is that we could not account for sex differences. To enable sufficient numbers and ages, given housing and breeding constraints (Burmeister et al. 2022), we used male and female goats from the Translational Research Unit (TRU) goat herd at University College Dublin Lyons Research Farm. This led to different numbers of male and female goats in each group. Despite this limitation, our data exhibit high coefficients of determination (R^2). This suggests that our methods were sufficiently robust to capture the

dynamics of postnatal bone development. Our ability to get consistent results is in agreement with the benefits of using genetically diverse populations in bone research (Migotsky et al. 2024). In future studies, we aim to directly interrogate sex as a biological variable among animals of more homogenous backgrounds (Nelson and Megyesi 2004).

5.0. Acknowledgements

6.0 Author contributions

Concept/design: CJP, MCL, PAJB, JDB, NCN. Acquisition of data: CJP, ME, EB, AW. Data analysis/interpretation: CJP, ME, EB, AW, PAJB, JDB, NCN. Drafting of the manuscript: CJP, PAJB, JDB, NCN. Critical revision of the manuscript: CJP, ME, EB, AW, KV, MCL, PAJB, JDB, NCN. Approval of the article: CJP, ME, EB, AW, KV, MCL, PAJB, JDB, NCN.

References

Acquaah, F., Robson Brown, K.A., Ahmed, F., Jeffery, N. and Abel, R.L. 2015. Early trabecular development in human vertebrae: overproduction, constructive regression, and refinement. *Frontiers in endocrinology* 6, p. 67.

Bahney, C.S., Zondervan, R.L., Allison, P., et al. 2019. Cellular biology of fracture healing. *Journal of Orthopaedic Research* 37(1), pp. 35–50.

Beall, M.H., van den Wijngaard, J.P.H.M., van Gemert, M.J.C. and Ross, M.G. 2007. Amniotic fluid water dynamics. *Placenta* 28(8–9), pp. 816–823.

Berendsen, A.D. and Olsen, B.R. 2015. Bone development. *Bone* 80, pp. 14–18.

Biewener, A.A. 1989. Scaling body support in mammals: limb posture and muscle mechanics. *Science* 245(4913), pp. 45–48.

Blitz, E., Sharir, A., Akiyama, H. and Zelzer, E. 2013. Tendon-bone attachment unit is formed modularly by a distinct pool of Scx- and Sox9-positive progenitors. *Development* 140(13), pp. 2680–2690.

Bouxsein, M.L., Boyd, S.K., Christiansen, B.A., Guldberg, R.E., Jepsen, K.J. and Müller, R. 2010. Guidelines for assessment of bone microstructure in rodents using micro-computed tomography. *Journal of Bone and Mineral Research* 25(7), pp. 1468–1486.

Breeland, G., Sinkler, M.A. and Menezes, R.G. 2024. Embryology, Bone Ossification. In: *StatPearls*. Treasure Island (FL): StatPearls Publishing.

Burmeister, D.M., Supp, D.M., Clark, R.A., et al. 2022. Advantages and disadvantages of using small and large animals in burn research: proceedings of the 2021 research special interest group. *Journal of Burn Care & Research*.

Collins, J.M., Lang, A., Parisi, C., et al. 2024. YAP and TAZ couple osteoblast precursor mobilization to angiogenesis and mechanoregulation in murine bone development. *Developmental Cell* 59(2), p. 211–227.e5.

Cooper, C., Westlake, S., Harvey, N., Javaid, K., Dennison, E. and Hanson, M. 2006. Review: developmental origins of osteoporotic fracture. *Osteoporosis International* 17(3), pp. 337–347.

Cooper, K.L., Sears, K.E., Uygur, A., et al. 2014. Patterning and post-patterning modes of evolutionary digit loss in mammals. *Nature* 511(7507), pp. 41–45.

Ducher, G., Tournaire, N., Meddahi-Pellé, A., Benhamou, C.-L. and Courteix, D. 2006. Short-term and long-term site-specific effects of tennis playing on trabecular and cortical bone at the distal radius. *Journal of Bone and Mineral Metabolism* 24(6), pp. 484–490.

Einhorn, T.A. and Gerstenfeld, L.C. 2015. Fracture healing: mechanisms and interventions. *Nature Reviews. Rheumatology* 11(1), pp. 45–54.

Frost, H.M. 1994. Wolff's Law and bone's structural adaptations to mechanical usage: an overview for clinicians. *The Angle orthodontist* 64(3), pp. 175–188.

Gardner, E. and Gray, D.J. 1970. The prenatal development of the human femur. *The American journal of anatomy* 129(2), pp. 121–140.

Goodship, A.E. and Kenwright, J. 1985. The influence of induced micromovement upon the healing of experimental tibial fractures. *The Journal of Bone and Joint Surgery. British Volume* 67(4), pp. 650–655.

Gorissen, B.M.C., Wolschrijn, C.F., van Vilsteren, A.A.M., van Rietbergen, B. and van Weeren, P.R. 2016. Trabecular bone of precocials at birth; Are they prepared to run for the wolf(f)? *Journal of Morphology* 277(7), pp. 948–956.

Gosman, J.H. and Ketcham, R.A. 2009. Patterns in ontogeny of human trabecular bone from SunWatch Village in the Prehistoric Ohio Valley: general features of microarchitectural change. *American Journal of Physical*

Anthropology 138(3), pp. 318–332.

Gutierrez, H.L., Tsutsumi, R., Moore, T.Y. and Cooper, K.L. 2019. Convergent metatarsal fusion in jerboas and chickens is mediated by similarities and differences in the patterns of osteoblast and osteoclast activities. *Evolution & Development* 21(6), pp. 320–329.

Herberg, S., McDermott, A.M., Dang, P.N., et al. 2019. Combinatorial morphogenetic and mechanical cues to mimic bone development for defect repair. *Science Advances* 5(8), p. eaax2476.

Ireland, A., Rittweger, J., Schönau, E., Lamberg-Allardt, C. and Viljakainen, H. 2014. Time since onset of walking predicts tibial bone strength in early childhood. *Bone* 68, pp. 76–84.

Kegelman, C.D., Nijsure, M.P., Moharrer, Y., et al. 2021. YAP and TAZ promote periosteal osteoblast precursor expansion and differentiation for fracture repair. *Journal of Bone and Mineral Research* 36(1), pp. 143–157.

Khonsari, R.H., Olivier, J., Vigneaux, P., et al. 2013. A mathematical model for mechanotransduction at the early steps of suture formation. *Proceedings. Biological Sciences / the Royal Society* 280(1759), p. 20122670.

Killian, M.L. 2022. Growth and mechanobiology of the tendon-bone enthesis. *Seminars in Cell & Developmental Biology* 123, pp. 64–73.

Kozhemyakina, E., Lassar, A.B. and Zelzer, E. 2015. A pathway to bone: signaling molecules and transcription factors involved in chondrocyte development and maturation. *Development* 142(5), pp. 817–831.

Leinders, J.J.M. and Sondaar, P.Y. 1973. On functional fusions in footbones of ungulates. *Zeitschrift für Säugetierkunde : im Auftrage der Deutschen Gesellschaft für Säugetierkunde e.V* 39, pp. 109–115.

Liu, X.S., Sajda, P., Saha, P.K., Wehrli, F.W. and Guo, X.E. 2006. Quantification of the roles of trabecular microarchitecture and trabecular type in determining the elastic modulus of human trabecular bone. *Journal of Bone and Mineral Research* 21(10), pp. 1608–1617.

Magrini, S.H., Mossor, A.M., German, R.Z. and Young, J.W. 2023. Developmental factors influencing bone strength in precocial mammals: An infant pig model. *Journal of Anatomy* 243(1), pp. 174–181.

Matziolis, G., Tuischer, J., Kasper, G., et al. 2006. Simulation of cell differentiation in fracture healing: mechanically loaded composite scaffolds in a novel bioreactor system. *Tissue Engineering* 12(1), pp. 201–208.

McDermott, A.M., Herberg, S., Mason, D.E., et al. 2019. Recapitulating bone development through engineered mesenchymal condensations and mechanical cues for tissue regeneration. *Science Translational Medicine* 11(495).

Migotsky, N., Kumar, S., Shuster, J.T., et al. 2024. Multi-scale cortical bone traits vary in females and males from two mouse models of genetic diversity. *JBMR Plus* 8(5), p. ziae019.

Moore, T.Y., Rivera, A.M. and Biewener, A.A. 2017. Vertical leaping mechanics of the Lesser Egyptian Jerboa reveal specialization for maneuverability rather than elastic energy storage. *Frontiers in zoology* 14, p. 32.

Nelson, D.A. and Megyesi, M.S. 2004. Sex and ethnic differences in bone architecture. *Current osteoporosis reports* 2(2), pp. 65–69.

Nowlan, N.C. 2015. Biomechanics of foetal movement. *European Cells & Materials* 29, p. 1–21; discussion 21.

Opperman, L.A. 2000. Cranial sutures as intramembranous bone growth sites. *Developmental Dynamics* 219(4), pp. 472–485.

Ott, S.M. 2018. Cortical or trabecular bone: what's the difference? *American Journal of Nephrology* 47(6), pp. 373–375.

Palaiothodorou, D. and Vagenas, G. 2024. Inter-arm bone mass and size asymmetries in children tennis players are maturity status specific: a 9-month study on the effects of training time across pubertal change and somatic growth. *European Journal of Applied Physiology* 124(7), pp. 2081–2092.

Ryan, T.M. and Krovitz, G.E. 2006. Trabecular bone ontogeny in the human proximal femur. *Journal of Human Evolution* 51(6), pp. 591–602.

Sanchez-Lara, P.A., Carmichael, S.L., Graham, J.M., et al. 2010. Fetal constraint as a potential risk factor for craniosynostosis. *American Journal of Medical Genetics. Part A* 152A(2), pp. 394–400.

Saunders, J.W. 1948. The proximo-distal sequence of origin of the parts of the chick wing and the role of the ectoderm. *The Journal of Experimental Zoology* 108(3), pp. 363–403.

Skedros, J.G., Hunt, K.J. and Bloebaum, R.D. 2004. Relationships of loading history and structural and material characteristics of bone: development of the mule deer calcaneus. *Journal of Morphology* 259(3), pp. 281–307.

Skedros, J.G., Sorenson, S.M., Hunt, K.J. and Holyoak, J.D. 2007. Ontogenetic structural and material variations in ovine calcanei: a model for interpreting bone adaptation. *Anatomical Record* 290(3), pp. 284–300.

Sugimoto, Y., Takimoto, A., Akiyama, H., et al. 2013. Scx+/Sox9+ progenitors contribute to the establishment of the junction between cartilage and tendon/ligament. *Development* 140(11), pp. 2280–2288.

Summerbell, D., Lewis, J.H. and Wolpert, L. 1973. Positional information in chick limb morphogenesis. *Nature* 244(5417), pp. 492–496.

Ulrich, D., van Rietbergen, B., Laib, A. and Rüegsegger, P. 1999. The ability of three-dimensional structural indices to reflect mechanical aspects of trabecular bone. *Bone* 25(1), pp. 55–60.

Villacís Núñez, C.N., Ray, A.P., Cooper, K.L. and Moore, T.Y. 2022. Metatarsal fusion resisted bending as jerboas (Dipodidae) transitioned from quadrupedal to bipedal. *Proceedings. Biological Sciences / the Royal Society* 289(1984), p. 20221322.

Warden, S.J., Mantila Roosa, S.M., Kersh, M.E., et al. 2014. Physical activity when young provides lifelong benefits to cortical bone size and strength in men. *Proceedings of the National Academy of Sciences of the United States of America* 111(14), pp. 5337–5342.

Weatherholt, A.M. and Warden, S.J. 2018. Throwing enhances humeral shaft cortical bone properties in pre-pubertal baseball players: a 12-month longitudinal pilot study. *Journal of Musculoskeletal & Neuronal Interactions* 18(2), pp. 191–199.

Wolff, J. 1893. Das gesetz der transformation der knochen. *Deutsche Medizinische Wochenschrift* 19(47), pp. 1222–1224.

Xie, M., Gol'din, P., Herdina, A.N., et al. 2020. Secondary ossification center induces and protects growth plate structure. *eLife* 9.